CHEMISTRY OF MATERIALS
Cite This: Chem. Mater. 2019, 31, 2524−2534
Article
pubs.acs.org/cm

Electronic Structure and Performance Bottlenecks of $CuFeO_2$ Photocathodes

Chang-Ming Jiang,[†,‡,#] Sebastian E. Reyes-Lillo,[⊥] Yufeng Liang,[∥] Yi-Sheng Liu,[§] Guiji Liu,[†,‡] Francesca M. Toma,[†,‡] David Prendergast,[∥] Ian D. Sharp,[*,#] and Jason K. Cooper[*,†,‡]

[†]Joint Center for Artificial Photosynthesis, [‡]Chemical Sciences Division, [§]Advanced Light Source, and [∥]The Molecular Foundry, Lawrence Berkeley National Laboratory, Berkeley, California 94720, United States

[⊥]Departmento de Ciencias Físicas, Universidad Andres Bello, Santiago 837-0136, Chile

[#]Walter Schottky Institut and Physik Department, Technische Universität München, Garching 85748, Germany

Supporting Information

ABSTRACT: The path to realizing low-cost, stable, and earth-abundant photoelectrodes can be enabled through a detailed understanding of the optoelectronic properties of these materials by combining theory and experimental techniques. Of the limited set of oxide photocathode materials currently available, $CuFeO_2$ has emerged as a promising candidate warranting detailed attention. In this work, highly compact thin films of rhombohedral (3R) $CuFeO_2$ were prepared via reactive co-sputtering. Despite its 1.43 eV indirect band gap, a cathodic photocurrent of 0.85 mA/cm^2 was obtained at 0.4 V versus reversible hydrogen electrode in the presence of a sacrificial electron acceptor. This unexpected performance was related to inefficient bulk charge separation because of the ultrafast (<1 ps) self-trapping of photogenerated free carriers. The electronic structure of 3R-$CuFeO_2$ was elucidated through a combination of optical and X-ray spectroscopic techniques and further complemented by first-principles computational methods including a many-body approach for computing the O K-edge X-ray absorption spectrum. Through resonant inelastic X-ray scattering spectroscopy, the visible absorption edges of $CuFeO_2$ were found to correspond to Cu → Fe metal-to-metal charge transfer, which exhibits a high propensity toward self-trapping. Findings of the present work enable us to understand the performance bottlenecks of $CuFeO_2$ photocathodes and suggest feasible strategies for improving material limitations.

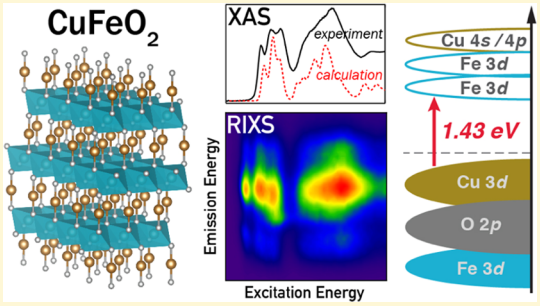

INTRODUCTION

Cu(I)-based semiconducting metal oxides, due to their native p-type conductivities, have garnered significant attention in recent studies of photoelectrochemical (PEC) solar fuel production.[1−3] The prototypical photocathode Cu_2O, with a 2 eV band gap, demonstrates excellent hydrogen production efficiency via solar water-splitting.[4−6] However, because the Cu_2O/Cu redox potential lies within the electronic band gap,[7] Cu_2O suffers from photocorrosion in aqueous environments and thus requires multilayer protection schemes.[8] Consequently, ternary oxides containing Cu(I) motifs have been investigated to allow for more versatile property design and optimization. Notably, the group of cuprous delafossite oxides ($Cu^+M^{3+}O_2$, M = Fe, Rh, Cr, Al, etc.) exhibits tunable optical band gaps and suitable conduction band energetic positions, making them promising photocathode candidates.[9−13] Among cuprous delafossites, $CuFeO_2$ possesses the smallest band gap ($E_g \approx 1.5$ eV), consists of earth-abundant elements, and can be prepared by various scalable and low-cost deposition methods.[13−21] The PEC stability of $CuFeO_2$ is also significantly improved compared with Cu_2O, which can be explained by its conduction band edge character. According to recent first-principles results, the lowest optical transition in $CuFeO_2$ is associated with Cu 3d + O 2p → Fe 3d charge transfer, thus greatly reducing the probability of Cu self-reduction.[22−25] Nonetheless, the unraveling of the detailed electronic structures of ternary oxides, including $CuFeO_2$ and other cuprous delafossites, is difficult to achieve experimentally. Conventional optical spectroscopy alone does not suffice for resolving and assigning the origins of various elementary excitations that define the absorption characteristics of such complex semiconductors. Given that $CuFeO_2$ offers a promising path to efficient and low-cost PEC solar fuels production, understanding of its fundamental properties (such as electronic structure and charge transport mechanisms) would provide guiding principles for further material design and optimization.

$CuFeO_2$ photocathodes exhibit catalytic activities that are highly dependent on the preparation methods. When fabricated by the Pechini sol−gel process, the material provides

Received: January 2, 2019
Revised: March 9, 2019
Published: March 11, 2019

DOI: 10.1021/acs.chemmater.9b00009
Chem. Mater. 2019, 31, 2524−2534

limited photovoltage and photocurrent density in the absence of sacrificial electron acceptors.[16−19] The poor hydrogen evolution reaction (HER) catalytic activity of $CuFeO_2$ is attributed to the high surface state density ($\sim 10^{14}$ cm^{-2}) that causes severe Fermi-level pinning at the semiconductor−liquid junction.[26] In comparison, $CuFeO_2$ photocathodes prepared by electrodeposition are capable of driving kinetically more challenging CO_2 reduction (CO_2R) reactions, with formate and acetate reported as the main products.[13−15] Nevertheless, whether such CO_2R catalytic activity stems from $CuFeO_2$ remains unclear because electrodeposited $CuFeO_2$ films often have complicated hollow morphologies and contain CuO as a secondary phase. Although the high surface area of electrodeposited $CuFeO_2$ benefits the PEC performance, discerning the role played by CuO in such photocathode assembly presents a challenge. In this work, we decouple the role of phase impurity from structural morphology through preparation of high-quality $CuFeO_2$ thin films with controllable secondary-phase contents via reactive co-sputtering. This method enables further examination of the fundamental optoelectronic properties and intrinsic PEC characteristics of the $CuFeO_2$ thin films.

The electronic structure of $CuFeO_2$ is studied by resonant inelastic X-ray scattering (RIXS) spectroscopy.[27] In this photon-in/photon-out technique, the incident X-ray resonantly promotes a core electron into a specific unoccupied level, which is sensitive to the local chemical environment. The relaxation of intermediate core excited states, detected in the form of X-ray emissions, provides insights into various elementary processes such as charge transfer, d−d, and phonon excitations.[28] The effectiveness of RIXS in resolving inherently the complex electronic structure of ternary oxides has been previously demonstrated on $BiVO_4$ and γ-$Cu_3V_2O_8$ photoanodes.[29−32] Herein, our O K-edge RIXS experiment is supported by first-principles calculations describing the distribution of each constituent element in $CuFeO_2$: the valence band maximum (VBM) comprises primarily Cu 3d states, whereas the conduction band minimum (CBM) is of nonbonding Fe 3d character. Furthermore, RIXS measurement at the Fe L-edge verifies that the visible absorption edges of $CuFeO_2$ are corresponding to Cu → Fe metal-to-metal charge transfer. The low bulk charge separation efficiency in $CuFeO_2$ as well as the observation of the long-lived excited state by transient absorption spectroscopy implies ultrafast electron self-trapping as being responsible for the low PEC performance. We also demonstrate that, while the presence of CuO enhances the CO_2R photocurrent density, phase-pure $CuFeO_2$ is an intrinsically poor catalyst for both HER and CO_2R. These results provide fundamental insights into the performance bottlenecks of $CuFeO_2$ photocathodes, inform strategies for improving PEC performance, and highlight the significance of interactions between different metals in multinary metal oxides.

EXPERIMENTAL SECTION

Preparation of $CuFeO_2$ Thin Films. Thin-film samples of rhombohedral (3R) $CuFeO_2$ were deposited on 50 × 50 mm^2 fluorine-doped tin oxide (FTO)-coated glass (TCO10-10, Solaronix) or 25 × 75 mm^2 quartz (CGQ-0640-01, Chemglass) substrates by magnetron co-sputtering in an LAB Line sputtering system (Kurt J. Lesker). Two radio frequency power supplies were separately controlled to manipulate the sputtering powers on circular (2″ diameter) Cu and Fe targets. In order to optimize the Cu/Fe ratio in the samples, the power on the Cu target was fixed at 32 W, while the Fe sputtering power was varied between 120 and 160 W. The working atmosphere consisted of 9 mTorr of inert Ar and 1 mTorr of O_2, and the substrate temperature was kept at 200 °C during the deposition process. The as-deposited samples underwent 6 h postannealing at 600 °C in a 1″ diameter quartz glass tube furnace under a flowing (180 sccm) Ar atmosphere.

Sample Characterization. The transition-metal compositions of the prepared $CuFeO_2$ thin films were quantified by inductively coupled plasma mass spectroscopy (7900 ICP−MS, Agilent) following digestion of films with concentrated HNO_3. The crystalline structures were analyzed by an X-ray diffractometer (SmartLab, Rigaku) using Cu Kα radiation at 0.5° grazing angle. Raman spectra were recorded using a confocal Raman microscope (LabRam HR, Horiba Jobin Yvon) with a 532 nm laser source. The excitation laser power at the sample surface was adjusted to be in the 1−2 mW range, and the spectral positions were calibrated by the characteristic Si phonon peak at 520.7 cm^{-1}. Film morphology and thickness were inspected using a scanning electron microscope (Quanta FEG 250, FEI). X-ray photoelectron spectroscopy (XPS) data were acquired by a Kratos Axis Ultra spectrometer using an Al Kα source ($h\nu$ = 1486.69 eV) operated at 225 W and a hemispherical electron energy analyzer. XPS binding energies were calibrated using adventitious alkyl carbon signals by shifting the C 1s peak to 284.8 eV. Optical transmission and specular reflection spectra were measured at 8° incident angle, using a UV−vis spectrometer equipped with an integrating sphere (SolidSpec-3700, Shimadzu) over the range from 300 to 1600 nm. Absorption coefficients and dielectric functions were obtained via spectroscopic ellipsometry using an M-2000DI ellipsometer (J. A. Woollam, Co.) with incident angle varying between 45° and 75° with 5° increments. Photothermal deflection spectroscopy (PDS) was collected on a home-built system in which monochromatic light from a laser stimulated light source (EQ-77, Enertiq) was modulated with an optical shutter and used for exciting the sample (immersed in perfluorohexane). The grazing probe beam was provided by a stabilized HeNe laser. Its position was detected with a position-sensitive detector, amplified and filtered with a current pre-amplifier, and then recorded with a lock-in amplifier.

PEC Measurements. The PEC measurements were conducted using an AM 1.5 solar simulator (16S-300-002, Solar Light) in a three-electrode configuration. A Pt wire served as the counter electrode, while a Ag/AgCl electrode immersed in 3 M KCl solution was used as the reference electrode. The pH 6.8 buffer solution consisted of 0.1 M $KHCO_3$ (Sigma-Aldrich) saturated with gaseous CO_2, with the option of adding 0.1 M $Na_2S_2O_8$ (Sigma-Aldrich) as a sacrificial electron scavenger. Current−voltage characteristics were recorded with a potentiostat (SP-300, Bio-Logic), and the reported potentials were converted to the reversible hydrogen electrode (RHE) scale using the following relation:

$$E_{RHE} = E_{Ag/AgCl} + 0.210\ V + (0.0591\ V) \times pH \quad (1)$$

The incident photon-to-current efficiency (IPCE) was measured with the presence of 0.1 M $Na_2S_2O_8$ at 0.40 V versus RHE external bias. A 150 W Xe arc lamp (M6255, Newport) combined with a holographic grating monochromator (CS-130, Oriel Instruments) was used to illuminate the front side of the $CuFeO_2$ photocathode, while differences in photocurrent and dark current responses at individual wavelength were acquired by a Gamry Reference 600 potentiostat. The reference incident spectrum was measured by recording the photocurrent response from a calibrated Si photodiode at 10 nm intervals between 330 and 850 nm. The IPCE data were then converted to absorbed photon-to-current efficiency (APCE) by dividing with (1 − transmission − reflection).

Transient Absorption Spectroscopy. Optical pump−optical probe transient absorption spectroscopy was performed using a 100 fs, 1 kHz, Ti:sapphire regenerative amplifier (Coherent Libra). A portion of the laser output was coupled to an optical parametric amplifier (Coherent OPerA Solo) for generating the 350 nm pump beam with a diameter of 0.3 mm and a pulse energy of 0.8 μJ at the sample. The supercontinuum probes in the visible and near-infrared regions were

DOI: 10.1021/acs.chemmater.9b00009
Chem. Mater. 2019, 31, 2524−2534

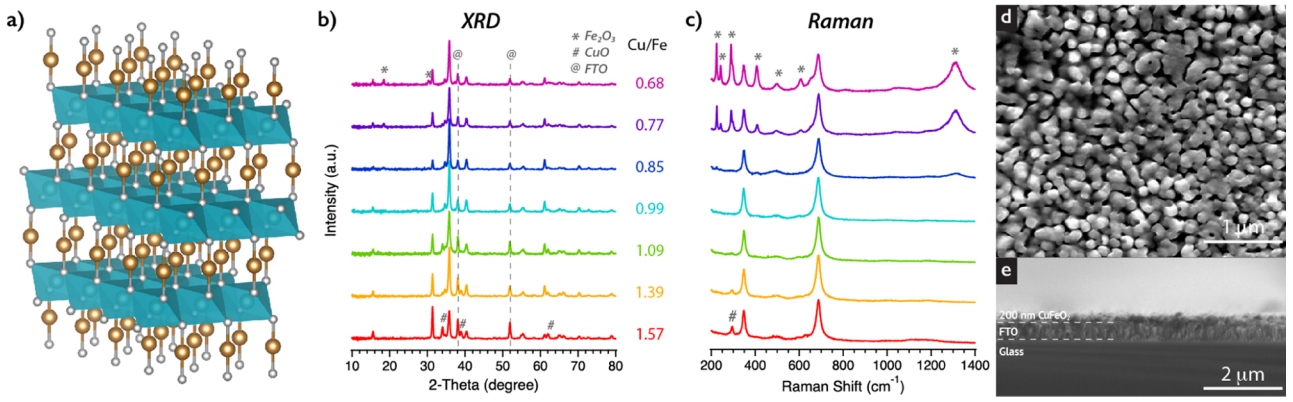

Figure 1. (a) Crystal structure of rhombohedral 3R-$CuFeO_2$. The Cu, Fe, and O atoms are given in brown, cyan, and gray, respectively. (b) XRD patterns and (c) Raman spectra of $CuFeO_2$ thin films with various Cu/Fe stoichiometric ratios. (d) Plane view and (e) cross-sectional view scanning electron microscopy (SEM) images of a 200 nm thick 3R-$CuFeO_2$ thin film prepared by reactive sputtering on an FTO-coated glass substrate.

generated using CaF_2 and a sapphire crystal, respectively. The incident angle of the probe beam was approximately 8° with respect to the sample surface normal. An Ultrafast Systems transient absorption system, equipped with two sets of fiber-coupled grating spectrometers plus Si CMOS detector arrays, was used for data collection. The two detectors were used for simultaneous collection of the differential transmission (dT) and the differential reflection (dR) signal. The differential absorption (dA) signal was calculated using the following equation[33]

$$dA = -\ln\left(\frac{\%\,T + \%\,R}{\%\,T\cdot 10^{dT} + \%\,R\cdot 10^{dR}}\right) \quad (2)$$

in which % T and % R are the ground-state transmission and reflectivity at 8° incident angle, respectively.

X-ray Spectroscopies. X-ray absorption (XAS), X-ray emission (XES), and RIXS measurements were performed at Beamline 8.0.1 of the Advanced Light Source, Lawrence Berkeley National Laboratory.[34] XAS spectra were recorded simultaneously in total electron yield (TEY) and total fluorescence yield (TFY) modes and normalized to the incoming photon flux, while being monitored by drain current measured from an upstream gold mesh. The incident energy resolution was set to be 100, 200, and 250 meV for the O K-edge, Fe L-edge, and Cu L-edge, respectively. TiO_2, Fe_2O_3, Cu, and CuO standards were used for XAS energy calibration. Emitted X-ray photons were energetically dispersed by a slit-less variable line-spacing spectrograph mounted at 90° to the incident photon beam direction and recorded by a charge coupled device detector (DO-936BN, Andor). The XES energy resolution was 250, 440, and 640 meV for the O K-edge, Fe L-edge, and Cu L-edge, respectively. RIXS experiments were performed with the same setup by varying incident X-ray photon energies for resonant excitation across different elemental edges.

First-Principles Calculations. Spin-polarized density functional theory (DFT) calculations were performed with Quantum ESPRESSO.[35,36] We use the generalized gradient approximation[37] plus Hubbard U (DFT + U) approach to properly describe the magnetic properties of $CuFeO_2$.[38,39] In order to account for the random spin orientation of the room-temperature paramagnetic phase of 3R-$CuFeO_2$, we used an antiferromagnetic (AFM) ordering with alternating in-plane spin orientation and zero total magnetization in a 2 × 2 × 1 supercell (48 atoms). We note that this AFM ordering differs from the low-temperature ground-state phase[40] and yields a structure with lower monoclinic symmetry ($C2/m$). Therefore, structural relaxations were performed with lattice constants fixed to their experimental values ($a = b$ = 3.0349 Å and c = 17.1656 Å for the primitive unit cell) until forces were smaller than 10^{-3} Ry/a.u. Our calculations of AFM 3R-$CuFeO_2$ use a kinetic energy cutoff of 30 Ry, a charge density cutoff of 300 Ry, 3 × 3 × 1 Γ-centered k-point grids and ultrasoft pseudopotentials with 11, 16, and 6 explicit valence electrons for Cu ($3d^{10}4s^1$), Fe ($3s^23p^63d^64s^2$), and O ($2s^22p^4$), respectively.[41] Projected density of states (PDOS) were computed using a denser 5 × 5 × 3 Γ-centered k-point grid. The band structure was computed along symmetry lines in the monoclinic setting.[42]

Many-body XAS spectra were simulated using the determinant formalism implemented in the ShirleyXAS and MBXASPY software codes.[43,44] Our calculations used a 2 × 2 × 1 supercell structure of the AFM ordering or, equivalently, a 4 × 4 × 1 supercell structure of the primitive cell (192 atoms). The supercell dimensions $a = b$ = 12.1396 Å and c = 17.1656 Å are sufficiently large to neglect effects from the core-hole impurity to neighboring periodic images. We use a temperature smearing of 0.3 eV, a 1 × 1 × 1 Γ-centered k-point grid and the same DFT parameters used for bulk calculations. The 1s core-excited O atom is simulated by a pseudopotential with the electronic configuration $1s^12s^22p^4$. Figure S13 shows several convergence studies performed for the XAS spectra on the k-point grid and supercell size (in all cases, the spectrum is averaged over spin-up and spin-down and in three dimensions). These DFT parameters result in excellent agreement with near-edge experimental measurements, as shown below in the Results section.

RESULTS AND DISCUSSION

$CuFeO_2$ can exist in rhombohedral (3R) or hexagonal (2H) polytypes, and most PEC applications have been developed on 3R-$CuFeO_2$, the crystal structure of which is shown in Figure 1a. Each Fe^{3+} is coordinated by six O^{2-} in slightly distorted FeO_6 octahedra. Edge-sharing FeO_6 layers stack along the c-axis alternatively with Cu^+ layers. The linear O−Cu−O units in $CuFeO_2$ resemble Cu_2O, a prototypical p-type oxide semiconductor.[4,6] In this study, $CuFeO_2$ thin films with varying Cu/Fe elemental ratios were deposited on FTO substrates by reactive co-sputtering. Following 6 h postdeposition annealing at 600 °C in an Ar atmosphere, X-ray diffraction (XRD) patterns of the prepared samples matched that of 3R-$CuFeO_2$ found in the ICDD database (Figures 1b and S1). Raman microspectroscopy (Figure 1c) also revealed the signatures of E_g and A_{1g} phonon modes of 3R-$CuFeO_2$ at 348 and 688 cm^{-1}, respectively.[45] A secondary α-Fe_2O_3 phase was detected in Raman spectra when Cu/Fe ratios (quantified by ICP−MS) were smaller than 0.85. This result is consistent with the previously reported phase segregation phenomenon in Fe-rich $CuFeO_2$ thin films prepared by the sol−gel process.[46] When Cu/Fe ratios were greater than 1.09, a secondary CuO phase was characterized by the XRD peaks at 34.0, 38.9, and 62.0°, as well as the Raman shift at 296 cm^{-1}. Within the composition

DOI: 10.1021/acs.chemmater.9b00009
Chem. Mater. 2019, 31, 2524−2534

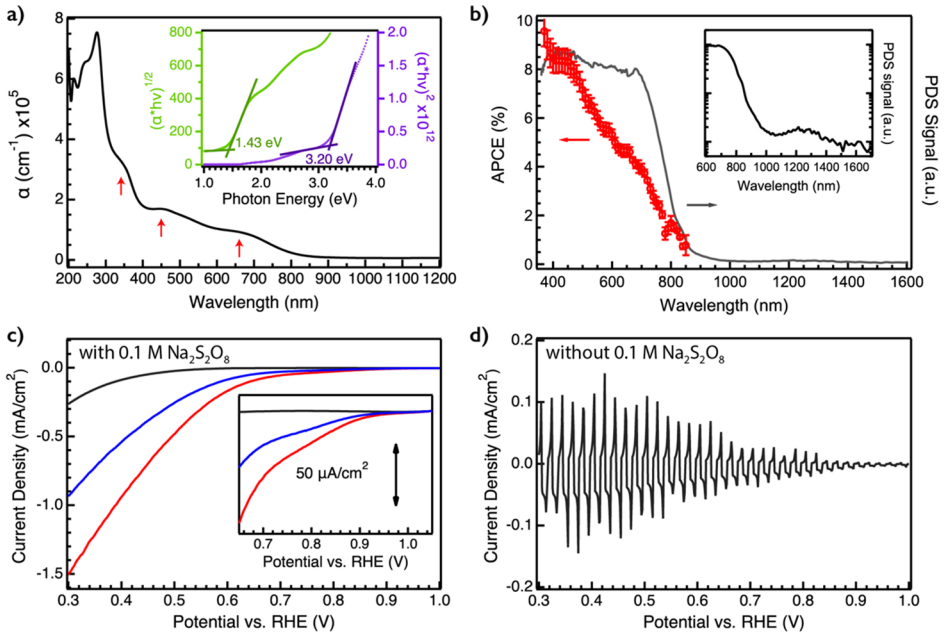

Figure 2. (a) Absorption coefficients of 3R-$CuFeO_2$ as a function of wavelength. Inset: Tauc plots for indirect (green) and direct (purple) allowed transitions. (b) APCE (red) and PDS (gray) profiles of $CuFeO_2$. APCE was measured at 0.4 V vs RHE with 0.1 M $Na_2S_2O_8$ as a sacrificial electron scavenger. Inset: PDS signal plotted in log scale in order to highlight the mid-band gap absorption feature. (c) Linear sweep voltammetry (LSV) measurement of a $CuFeO_2$ photocathode under dark condition (black), front-side (red), and back-side (blue) illumination in the presence of 0.1 M $Na_2S_2O_8$. The scan rate was 50 mV/s in the cathodic direction. (d) LSV measurement of a $CuFeO_2$ photocathode under chopped front-side illumination at 20 mV/s scan rate without the addition of $Na_2S_2O_8$.

window of Cu/Fe ratios between 0.85 and 1.09, no evidence for secondary phases was observed. These phase-pure 3R-$CuFeO_2$ thin films enable the study of fundamental optoelectronic properties and intrinsic PEC characteristics.

As shown in the SEM images (Figure 1d–e), our sputtered $CuFeO_2$ formed a uniform coverage with nanoporous morphology, which could be attributed to the rough surface of FTO substrates. When deposited on a quartz substrate with the same sputtering procedure, the resulting $CuFeO_2$ layer was more continuous and the intensity of the (012) diffraction peak increased (Figure S1). It should be noted that the desired 3R-$CuFeO_2$ phase on FTO glass was only obtained at 600 °C annealing temperature (Figure S2). The transformation from the as-grown films to 3R-$CuFeO_2$ was not achieved at 550 °C or lower temperatures. At above 650 °C, Fe_2O_3 peaks can be observed in the Raman spectra even for stoichiometric films, suggesting the decomposition of $CuFeO_2$ at higher temperatures. In comparison, on quartz substrates, annealing to 650 °C was required to achieve conversion to the delafossite phase, and no decomposition was observed at 700 °C (Figure S2).

The transmission and reflectivity spectra measured from a phase-pure 3R-$CuFeO_2$ sample on FTO glass are shown in Figure S3, and the clear absorption onset at 880 nm matched the previously reported band gap values.[13,16] To mitigate light scattering and reflection from the rough FTO layer, spectroscopic ellipsometry was performed instead on a $CuFeO_2$ sample deposited on quartz (fitting results in Figure S4) to extract the refractive index (n), extinction coefficient (k), and absorption coefficient (α). As shown in Figure 2a, 3R-$CuFeO_2$ exhibits significant absorption in the visible wavelengths, with $\alpha \approx 1 \times 10^5$ cm^{-1} at 600 nm. Tauc analysis indicated that the indirect and direct allowed band gaps are 1.43 and 3.20 eV, respectively. For many cuprous delafossites, a strong and narrow absorption peak can be found between 3.7 and 4.5 eV.[23,47] This feature has been assigned to the first excitonic peak of the direct allowed Cu 3d + O 2p → Cu 4s transition, enabled by the linear O–Cu–O structure. Thus, in the current study, the sharp absorption feature at 280 nm (~4.4 eV) is referred as the Cu 3d + O 2p → Cu 4s exciton peak. Although Tauc analysis is generally not valid for excitonic transitions, the band gap assignment of $CuFeO_2$ was not affected because the exciton peak is located far from both the direct and indirect band gaps. Three broader absorption features at 340, 450, and 660 nm can also be distinguished in Figure 2a, and the optical excitation pathways associated with these features will be investigated by RIXS and discussed later in this work. PDS, which detects the heat dissipated from the sample through nonradiative recombination,[48] also revealed a sharp absorption onset at 880 nm (Figure 2b). The extended absorption character at ~900 nm can be related to defect-related tail states. We relate the broad absorption peak at ~1250 nm (0.99 eV) to absorption from on-site Fe d–d excitations, which is further confirmed by Fe L-edge RIXS, as discussed below.

PEC performances of the sputtered $CuFeO_2$ thin films were tested in pH 6.8 buffer (0.1 M $KHCO_3$ solution constantly saturated with CO_2 gas) using a simulated AM 1.5 solar spectrum at 100 mW/cm^2 intensity. When 0.1 M $Na_2S_2O_8$ was added as the sacrificial electron acceptor, the phase-pure $CuFeO_2$ photocathode with a ~1:1 Cu/Fe ratio showed a cathodic photocurrent onset at 0.92 V versus RHE, and the photocurrent density increased sharply at 0.6 V versus RHE, eventually reaching 0.85 mA/cm^2 at 0.4 V versus RHE (Figure 2c). These characteristics are similar to those measured from phase-pure $CuFeO_2$ electrodes prepared by the sol–gel process[16] or electrodepositon[13] measured in 1 M NaOH with O_2 gas as the sacrificial electron acceptor. If no sacrificial reagent was present in the electrolyte, only ~50 μA/cm^2

DOI: 10.1021/acs.chemmater.9b00009
Chem. Mater. 2019, 31, 2524–2534

photocurrent density was obtained from the same photocathode (Figure 2d), suggesting that $CuFeO_2$ has very limited surface catalytic activity for either HER or CO_2R.

Figure S5 compares the PEC performances of $CuFeO_2$ thin films with different Cu/Fe ratios. When $Na_2S_2O_8$ was present, no systematic change in photocurrent amplitude was observed. In the absence of the sacrificial reagent, $CuFeO_2$ photocathodes with higher Cu/Fe ratios (i.e. with the CuO secondary phase) exhibited three times higher photocurrent densities. On these Cu-rich $CuFeO_2$ photocathodes, an additional reduction (oxidation) half-wave was observed at ~0.6 V (~0.8 V) versus RHE in the cyclic voltammetry scan, which can be attributed to the Cu^{2+} redox process from the CuO secondary phase. Therefore, the higher photocurrents obtained from these photocathodes were not indicative of intrinsically improved catalytic activity, but rather CuO (or its in situ reduced form) acting as the catalyst atop the $CuFeO_2$ light absorber. This observation partly explains the CO_2R catalytic activity difference between $CuFeO_2$ photocathodes prepared by sol–gel or electrodeposition methods, where CuO phase segregation is typical. Although beyond the scope of the present work, further understanding of the interplay between $CuFeO_2$ and CuO would help facilitate the development of efficient PEC CO_2R systems.

Even with the sacrificial electron acceptor, photocurrents generated from $CuFeO_2$ photocathodes were more than 1 order of magnitude lower than the theoretical limit; considering the absorption characteristics of $CuFeO_2$ (200 nm thickness) and the photon flux of the AM 1.5 solar spectrum, a maximum photocurrent of 24.2 mA/cm^2 is expected (Figure S6). The onset of the APCE, measured at 0.4 V versus RHE in the presence of $Na_2S_2O_8$, occurred at 850 nm, which is similar to the optical absorption onset determined by PDS (Figure 2b). However, while the PDS signal quickly reached a plateau at 700 nm, the APCE profile increased more gradually and barely surpassed 10% at 400 nm. This suggests that a large percentage of photogenerated charge carriers undergo bulk recombination instead of being collected at the semiconductor–liquid junction. Moreover, the observation of lower photocurrent when illuminated from the backside of the photoelectrode (Figure 2c) also points to the minority carrier (electron) diffusion length being a primary performance-limiting factor.

The bulk carrier transport limitation of $CuFeO_2$ is not only evidenced through PEC measurements but also complemented by time-resolved optical spectroscopy. Figure 3a represents the differential transmission (dT) spectra at various time delays following an optical excitation. As previously studied in the case of $BiVO_4$ photoanodes,[33] the derivative-like features near the optical transitions originate from shifting and broadening of oscillators, while the broad negative background in the near-infrared range (>1000 nm) is related to the free carrier absorption. The actual differential absorption (dA) signal was reconstructed by collecting both differential transmission and differential reflectivity simultaneously, and the free carrier lifetime in $CuFeO_2$ was found to be extremely short. As shown in Figure 3b, a biexponential decay model gave an excellent fit to the dA signal measured at 1100 nm, with decay time constants being 0.22 ± 0.01 and 4.40 ± 0.28 ps. It should be noted that time-resolved microwave conductivity measurement, which probes conducting charge carriers (as opposed to free carriers), yields a much longer (200 ns) lifetime.[26] Comparison of these results suggests that the photogenerated

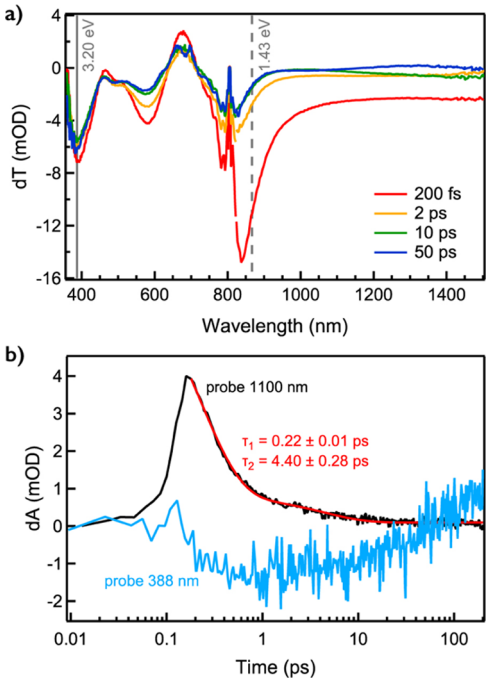

Figure 3. (a) Differential transmission (dT) spectra of $CuFeO_2$ (200 nm on quartz) at various pump–probe delays. Excitation wavelength: 350 nm, power: 0.8 μJ/pulse, beam diameter ~0.3 mm. (b) Time dependence of the differential absorption (dA) signal at 1100 nm (black) or 388 nm (blue) probe wavelengths. The red line indicates the biexponential decay fitting result to the 1100 nm dA data.

free carriers may quickly self-trap and form small polarons by distorting the surrounding lattice. Thus, it is likely that polaronic transport serves as the dominating conduction mechanism in $CuFeO_2$, as in a range of other transition-metal oxides.[49−52] Indeed, inspection of dT spectra (Figure 3a) reveals that the feature near 388 nm, associated with the direct band gap (3.20 eV), persisted to much longer times than the rapidly relaxing spectral response in the near-infrared. Moreover, the reconstructed 388 nm dA signal exhibited a rise that correlated well with the rapid decay of the free carrier signal at 1100 nm, and then subsequently persisted for tens of picoseconds (Figure 3b), thus indicating a long-lived excited state that may be associated with the existence of electrons or hole polarons. Even though the excitation energy density used in this measurement was much higher than the 1 sun intensity for PEC performance evaluation, it is worth noting that higher-order phenomena, such as Auger recombination, can be ruled out as the signal intensity was linear with excitation energy (Figure S7). Previously, Prévot et al. reported that a surface hydroxide layer of $CuFeO_2$ promotes charge recombination and reduces photovoltage.[26] Our findings suggest, in addition to the detrimental surface states, that poor bulk charge transport also warrants further attention. To realize the full potential of $CuFeO_2$ as a photocathode, the surface states need to be effectively passivated and the charge diffusion length must be improved to be comparable with the absorption depth.

To obtain further insight into the room-temperature electronic structure of 3R-$CuFeO_2$, we performed zero-temperature spin-polarized DFT + U calculations for an AFM spin arrangement of 3R-$CuFeO_2$ (see Experimental Section for details). At this level of theory, electronic structure calculations are sensitive to the Hubbard U value chosen for

DOI: 10.1021/acs.chemmater.9b00009
Chem. Mater. 2019, 31, 2524−2534

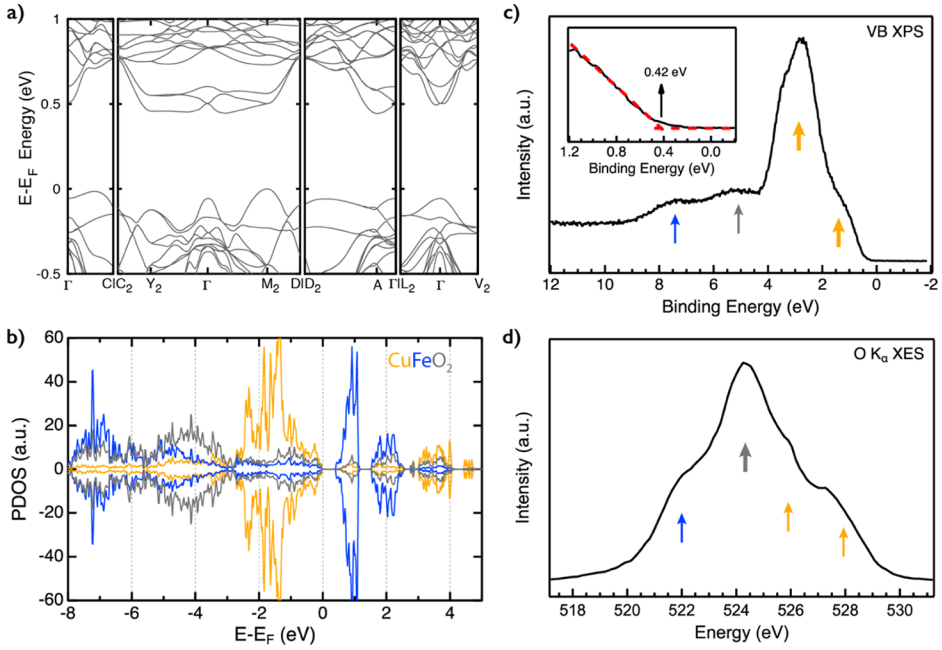

Figure 4. (a) Band structure calculation for 3R-$CuFeO_2$ using DFT + U with U = 2 eV for Fe. The room-temperature paramagnetic phase of 3R-$CuFeO_2$ was simulated using an AFM spin ordering. (b) PDOS calculations for 3R-$CuFeO_2$ using DFT + U. Colors denote Cu (yellow), Fe (blue), and O (gray) orbital contribution. The Fermi level is set at the highest occupied state. (c) Experimental valence band XPS spectrum of $CuFeO_2$. Inset: The enlarged valence band onset region. (d) Experimental O Kα nonresonant XES spectrum. Arrows indicate the contributions from Cu (yellow), Fe (blue), and O (gray) PDOS.

the on-site correlation. In this work, a Hubbard U value of 2 eV was chosen for Fe ions to approximate the experimental crystal field splitting. However, we note that varying the U value from 1 to 3 eV has a negligible qualitative impact on the calculated PDOS (Figure S8). Because Cu^+ has a closed d-shell configuration, a Hubbard U value correction has a negligible effect on the computed spectrum.[53] The band structure shown in Figure 4a confirms the indirect band gap of $CuFeO_2$—the VBM and the CBM are located at the M_2 and the A points of the Brillouin zone, respectively. The calculated 0.444 eV band gap severely underestimated the experimental value by 70%. The disagreement on band gap is not uncommon at this level of theory and is largely explained by strong on-site correlation effects arising from the frontier Fe 3d orbitals. According to the band structure, the electron and hole effective masses were found to be $1.828m_0$ and $1.348m_0$, respectively, although effective masses are expected to display small variations with the level of theory. PDOS for Cu, Fe, and O are shown in Figure 4b, and the results are in good agreement with previous DFT + U calculations for $CuFeO_2$.[23,53,54] The VBM is dominated by Cu 3d states (Figure S9), with some degree of hybridization with O 2p. The occupied O 2p and Fe 3d states were found to be 4.5 and 7 eV away from the VBM, respectively. The CBM was found to consist of mainly Fe 3d states, with a ∼1.1 eV crystal-field splitting due to the octahedral O coordination around Fe ions. Unoccupied Cu 4s and 4p states are located at ∼2.5 eV above the CBM.

The computed PDOS provides guidance for the analysis of a combination of soft X-ray spectroscopies that probe the valence and conduction bands. Starting with probes of the valence band, XPS revealed that the Fermi level at the surface is located 0.42 eV above VBM, which is consistent with the p-type conductivity of $CuFeO_2$ (Figure 4c). At least four peaks were resolved and matched well with the calculated PDOS distribution in Figure 4b. The peaks related to Cu 3d states were of higher amplitudes because with the Al Kα radiation ($h\nu$ = 1486.69 eV) used in the XPS measurement, the photoionization cross section for Cu 3d electrons is ∼50 and ∼5.5 times larger than that for the O 2p and Fe 3d electrons, respectively.[55] In comparison, nonresonant O Kα XES spectroscopy also revealed four peaks, but with the main peak (524.5 eV) located ∼5 eV below the emission onset (Figure 4d). Because XES detects the radiative recombination between a core-hole and a valence electron, it carries higher element specificity toward O PDOS in the valence band, with the PDOS of Cu and Fe still visible as the weak shoulders flanking the main emission peak.

XAS acquired in TFY mode is more bulk-sensitive and was used to probe the unoccupied levels in the conduction band. At the Cu L_3-edge, $CuFeO_2$ exhibited a broad absorption peak at 934 eV (Figure S10). These results, in conjunction with the Cu 2p XPS emission shown in Figure S11, support the Cu-oxidation state in $CuFeO_2$ to be +1.[56,57] At the Fe L-edge XAS, $CuFeO_2$ exhibited a doublet with 1.60 eV separation (Figure S10), similar to Fe_2O_3, which is related to the d-orbital manifold (t_{2g} and e_g) in the octahedral ligand field.[58] In the O K-edge XAS (Figure S10), three absorption peaks (530.6, 532.1, and 533.7 eV) were resolved in the pre-edge region, originating from hybridization between oxygen and metals. The energy positions and separation (∼1.3 eV) between the first two absorption peaks of $CuFeO_2$ resemble the doublet peaks measured from an Fe_2O_3 reference and are related to the Fe 3d states.[59] When compared with the conduction band PDOS (Figure 4b), the third pre-edge absorption peak at 533.7 eV can be reasonably assigned to hybridized Cu 4s/4p states.

To support our assignments of the XAS spectrum and provide deeper fundamental insights into the optoelectronic properties of $CuFeO_2$, first-principles many-body XAS

DOI: 10.1021/acs.chemmater.9b00009
Chem. Mater. 2019, 31, 2524−2534

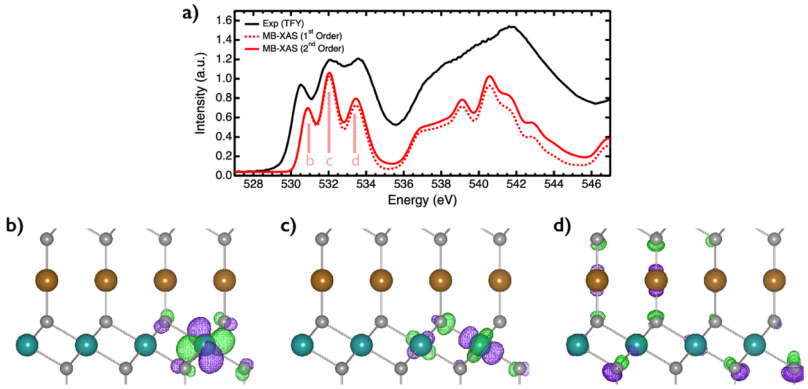

Figure 5. (a) Experimental versus theoretical XAS spectrum of 3R-$CuFeO_2$. The computed spectrum, obtained with the determinant formalism, is averaged over spin-up and spin-down AFM configurations and in three dimensions. Note that the energy axis is shifted for the calculated spectrum in order to give a better comparison to the experimental data. (b–d) Probability densities of the final-state wavefunctions for the three pre-edge peaks at the O K-edge. Wavefunction orbitals for spin-up and spin-down are equivalent, therefore only the spin-up case is shown in the figure. The Cu, Fe, and O atoms are given in brown, cyan, and gray, respectively.

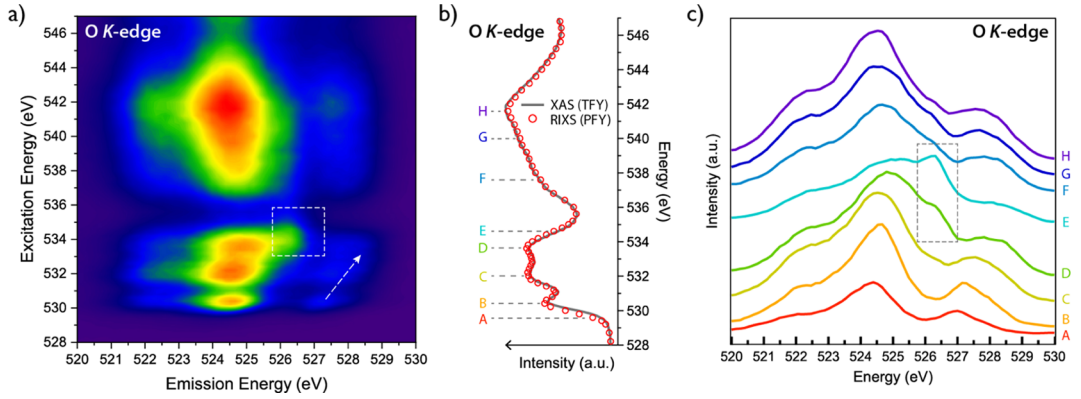

Figure 6. (a) RIXS mapping results at the O K-edge. (b) XAS spectrum of $CuFeO_2$ at the O K-edge (black line) and integrated O Kα XES intensity as a function of excitation energy (red circles). (c) Selected XES spectra with excitation energies labeled in accordance with panel (b).

calculations were performed on the AFM configuration with the determinant formalism to simulate the room-temperature 3R-$CuFeO_2$.[43,44] The calculated O K-edge XAS spectrum for the AFM configuration agrees well with the experimental data (Figure 5a), supporting the accuracy of the DFT modeling of the conduction band PDOS in the paramagnetic phase. The position and relative magnitude of the three pre-edge absorption peaks are clearly reproduced at this level of theory. First- and second-order excitations are shown to emphasize that many-body effects can lead to peak intensity increase at higher energies above the absorption onset. Alternatively, XAS spectra computed for ferromagnetic (FM) and nonmagnetic (NM) ordering of 3R-$CuFeO_2$ are shown in Figure S14. The AFM state corresponds to the lowest total-energy structure; the FM and NM configurations are 53.9 and 1464.2 meV per formula unit above the AFM configuration, respectively. While the computed XAS spectra for the FM and NM configurations display similarities with the experimental results, these magnetic orderings correspond to metastable states and are therefore disregarded. This determinant formalism further enables plotting of the probability densities of the final-state wavefunctions associated to the three pre-edge oscillators, as shown in Figure 5b–d. The orbital projections suggested that the CBM of $CuFeO_2$ consists of Fe 3d nonbonding states, while the higher-energy Fe states exhibit a certain degree of Fe–O antibonding character. The highest pre-edge peak is mainly associated with antibonding Cu sp hybrid orbitals, but also involves Fe–O antibonding interactions. With this information on the conduction band PDOS distribution, we then performed RIXS at the O K-edge in order to investigate the nature of various band-to-band transitions in $CuFeO_2$.

Figure 6a gives a two-dimensional plot of the O K-edge emission spectra as a function of X-ray excitation energy. For each excitation energy, the integrated X-ray emission intensity gave a measure of XAS strength in the form of partial fluorescence yield (PFY). It can be seen in Figure 6b that the reconstructed PFY-XAS spectrum matches well with the scanning TFY result. Eight representative O K-edge resonant XES spectra are plotted and compared in Figure 6c. A blue shift of the XES onset can be observed when the excitation moves from CBM to higher photon energies, indicating that the VBM and CBM are not aligned in k-space and the optical band gap is an indirect transition.[60] When the X-ray excitation resonantly excites a core electron into the unoccupied Fe 3d levels near the CBM (530.6 and 532.1 eV), the corresponding X-ray emission carries more weight from the occupied Fe 3d levels near the bottom of the valence band (522 eV). A narrow emission peak at 526.4 eV was only observed with excitation energy between 533 and 535 eV, corresponding to excitation into the Cu 4s/4p states. This result confirms that the VBM consists of occupied Cu 3d states, as also supported by XPS, non-resonant O Kα XES, and first-principles calculation.

DOI: 10.1021/acs.chemmater.9b00009
Chem. Mater. 2019, 31, 2524–2534

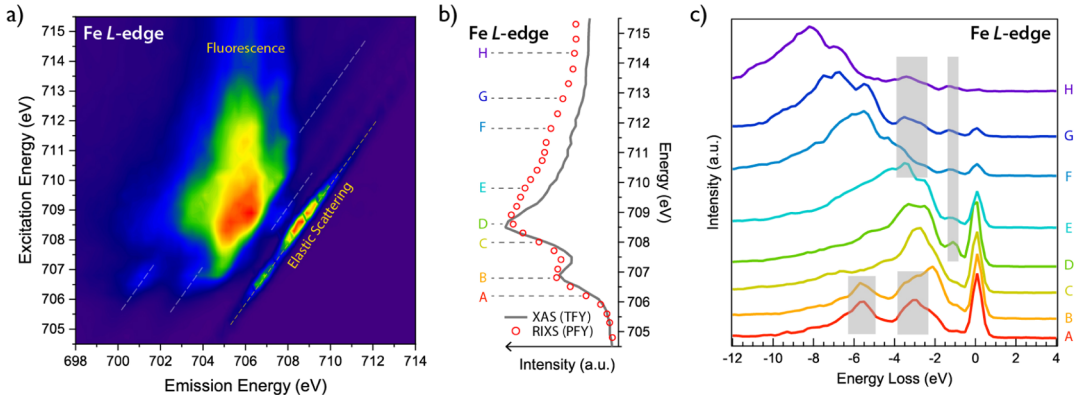

Figure 7. (a) RIXS mapping results at the Fe L-edge. Dashed lines indicate the inelastic scattering peaks. (b) XAS spectrum of $CuFeO_2$ at the Fe L-edge (black line) and integrated Fe Lα XES intensity as a function of excitation energy (red circles). (c) Selected XES spectra with excitation energies labeled in accordance with panel (b). The energy loss x-scale is defined relative to the excitation energy.

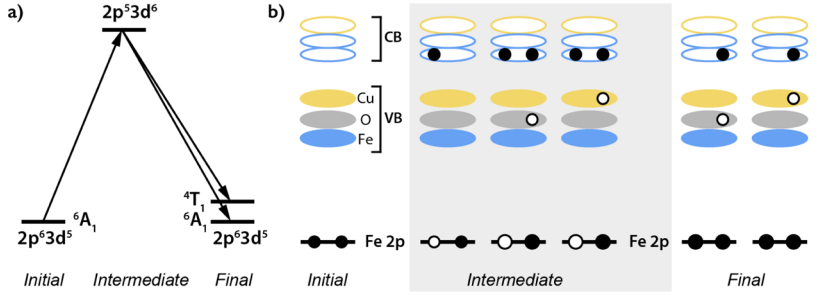

Figure 8. (a) Schematic energy-level diagram of the Fe L-edge RIXS process leading to the $^4T_1$ d−d excited state. (b) Schematic diagram of the charge transfer processes in the intermediate state of the Fe L-edge RIXS.

RIXS measurement was also performed at the Fe L-edge. Following excitation of an Fe 2p electron into the conduction band, the resulting X-ray emission spectra also exhibit a clear dependence on the excitation energy (Figure 7). In addition to the nonresonant fluorescence peak at 705.5 eV, a few features with constant energy loss from the excitation energy were observed (dashed lines in Figure 7a). Figure 7c plots selected X-ray emission spectra with respect to the energy loss scale, and three inelastic scattering peaks were located at ∼1.0, ∼3.1, and ∼5.6 eV. For strongly correlated materials, such as many transition-metal oxides, the energy losses of this range are typically indicative of d−d or charge transfer excitations.[28] A similar 1 eV energy-loss feature has also been reported on single crystal and nanorods of α-Fe_2O_3, which adopts the same octahedral FeO_6 local symmetry.[61,62] One plausible origin for this 1 eV energy loss is the d−d excitation of Fe^{3+}. As depicted in Figure 8a, the initial (ground) state of an octahedrally coordinated high-spin Fe^{3+} is $^6A_1$. Following a resonant Fe L-edge excitation, an additional electron is placed in the Fe 3d level, while a core-hole is created at the Fe 2p level, leading to the $2p^53d^6$ intermediate state. The elastic scattering process would recreate the ground $^6T_1$ state by emitting an X-ray photon with the same energy as the excitation photon. However, the relaxation of the intermediate state can also result in an Fe^{3+} cation with other electronic configurations, such that the final state differs from the initial state via a d−d excitation. Given that this energy-loss feature was most pronounced when the X-ray excitation aligned with the Fe e_g level absorption (708.5 eV), it is likely that the associated final state is $^4T_1$, which would require 1 eV to excite a t_{2g} electron into the e_g level. We would like to note that a sub-band gap absorption feature at 0.99 eV (1250 nm) was also observed on $CuFeO_2$ by PDS (Figure 2b), which also agrees well with the 1 eV energy-loss feature detected by the Fe L-edge RIXS. This type of on-site d−d excitations only changes the local electronic configuration, but does not contribute to conducting charge carriers that are required for PEC use.

The inelastic scattering peaks at ∼3.1 and ∼5.6 eV energy losses are assigned as charge transfer excited states. Specifically, the ∼5.6 eV feature corresponds to O → Fe ligand-to-metal charge transfer, while the broad feature at ∼3.1 eV is related to Cu → Fe metal-to-metal charge transfer. Even though electronic transitions involving core levels are highly element-specific, the hybridization between Fe, O, and Cu enables charge transfer between different elements in the intermediate state (Figure 8b). Consequently, the resulting final states would be equivalent to the optically excited $CuFeO_2$ semiconductor, and the energy losses in the X-ray scattering process are equivalent to the valence-to-conduction band transition energies. According to the PDOS alignment in Figure 4b, the 5.6 eV energy loss in RIXS can be achieved by charge transfer from the O 2p states within the valence band to the CBM, which is of Fe 3d character. On the other hand, a correlation can be drawn between the 3.1 eV Fe RIXS energy-loss feature and the absorption coefficient (α) spectrum obtained by spectroscopic ellipsometry (Figure S15). Under closer inspection, the broad energy-loss peak between 1.5 and 3.8 eV seems to comprise several overlapping peaks that match well with the absorption edges of $CuFeO_2$ at 340, 450, and 660 nm (3.65, 2.76, and 1.88 eV). Because the valence band edge mainly consists of Cu 3d states, we can confidently suggest that Cu-to-Fe charge transfer is responsible for the visible

DOI: 10.1021/acs.chemmater.9b00009
Chem. Mater. 2019, 31, 2524−2534

absorption of $CuFeO_2$, as well as the ~3.1 eV energy-loss feature measured at the Fe L-edge. This finding implies that photogenerated electrons and holes separate at the atomic scale near the Fe and Cu cations, respectively, which should suppress direct electron−hole recombination because there is no direct covalent bonding between these elements. However, APCE shows that $CuFeO_2$ photocathodes suffer from poor bulk charge separation, especially in the visible wavelengths (Figure 2b), which may be a consequence of charge localization via small polaron formation at these sites. In addition, to reduce charge transport limitations and improve the efficiency of $CuFeO_2$ photocathodes, anisotropies arising from the delafossite structure should also be taken into account. In particular, given the alternating CuO_2 and FeO_6 layers in the lattice, controlled growth perpendicular to the *c*-axis would enable out-of-plane transport along extended Cu and Fe planes, which is expected to benefit charge collection.

CONCLUSIONS

In summary, we have achieved phase-pure thin films of p-type 3R-$CuFeO_2$ by reactive co-sputtering. The PEC performance in 0.1 M $Na_2S_2O_8$ demonstrated an onset potential of 0.92 V versus RHE and 0.85 mA/cm^2 photocurrent density at 0.4 V versus RHE. Optical characterization indicates indirect and direct band gaps of 1.43 and 3.20 eV, respectively. The nonoptimal PEC characteristics of $CuFeO_2$, largely limited by electron transport, were manifested by the 3% (10%) APCE at 750 nm (400 nm). This is further supported by the ultrafast relaxation (<1 ps) of photogenerated free carriers, accompanied by the appearance of a longer-lived excited state, suggesting the possibility of small polaron formation. Moreover, the enhanced CO_2R photocurrent densities exhibited by Cu-rich photocathodes were originated from the secondary CuO phase rather than an intrinsic catalytic activity of $CuFeO_2$. The electronic structure was elucidated through a combination of experimental X-ray spectroscopies including XAS, XES, XPS, and RIXS. This is further complemented by first-principles computational methods including a many-body approach for computing the O K-edge XAS spectrum. The VBM is found to be primarily of Cu 3d character, whereas the CBM consists of nonbonding Fe 3d states. Considering the alternating CuO_2 and FeO_6 planes in the delafossite lattice, effective charge transport is likely severely limited and thus leads to significant charge recombination in these polycrystalline films. This is likely reflected in the poor fill factor observed in PEC and the larger potentials required achieving electron hole separation. In developing new ternary metal oxides for PEC applications, most efforts have been guided by physical properties such as optical band gap and operational stability. The results of the present work underscore the significance of interactions between different metals as well. Further optimization efforts are likely to significantly benefit from heteroepitaxial growth along the direction perpendicular to the delafossite *c*-axis.

ASSOCIATED CONTENT

Supporting Information

The Supporting Information is available free of charge on the ACS Publications website at DOI: 10.1021/acs.chemmater.9b00009.

XRD patterns, Raman spectra, variable angle spectroscopic ellipsometry data and fit results, *J*−*E* characteristics of $CuFeO_2$ thin films with different Cu/Fe ratios, theoretical cumulative photocurrent, calculated PDOS by DFT + *U* using different Fe *U* values, XAS spectra at the O K-edge and Fe and Cu L-edges, XPS spectra of Cu 2p, Fe 2p, and O 1s levels, and work function measurement result (PDF)

AUTHOR INFORMATION

Corresponding Authors

*E-mail: sharp@wsi.tum.de (I.D.S.).
*E-mail: jkcooper@lbl.gov (J.K.C.).

ORCID

Chang-Ming Jiang: 0000-0001-8327-5760
Francesca M. Toma: 0000-0003-2332-0798
Ian D. Sharp: 0000-0001-5238-7487
Jason K. Cooper: 0000-0002-7953-4229

Notes

The authors declare no competing financial interest.

ACKNOWLEDGMENTS

This material is based upon work performed by the Joint Center for Artificial Photosynthesis, a DOE Energy Innovation Hub, supported through the Office of Science of the U.S. Department of Energy under Award Number DE-SC0004993. Theory and computational works were performed at The Molecular Foundry, which is supported by the Office of Science, Office of Basic Energy Sciences, of the U.S. Department of Energy under Contract no. DE-AC02-05CH11231. XAS, XES, and RIXS measurements were performed at the Advanced Light Source, which is also supported by the Office of Science, Office of Basic Energy Sciences, of the U.S. Department of Energy under Contract no. DE-AC02-05CH11231.

REFERENCES

(1) Sullivan, I.; Zoellner, B.; Maggard, P. A. Copper(I)-Based p-Type Oxides for Photoelectrochemical and Photovoltaic Solar Energy Conversion. *Chem. Mater.* **2016**, *28*, 5999−6016.

(2) Sivula, K.; van de Krol, R. Semiconducting Materials for Photoelectrochemical Energy Conversion. *Nat. Rev. Mater.* **2016**, *1*, 15010.

(3) Rajeshwar, K.; Hossain, M. K.; Macaluso, R. T.; Janáky, C.; Varga, A.; Kulesza, P. J. Review-Copper Oxide-Based Ternary and Quaternary Oxides: Where Solid-State Chemistry Meets Photoelectrochemistry. *J. Electrochem. Soc.* **2018**, *165*, H3192−H3206.

(4) Paracchino, A.; Laporte, V.; Sivula, K.; Grätzel, M.; Thimsen, E. Highly Active Oxide Photocathode for Photoelectrochemical Water Reduction. *Nat. Mater.* **2011**, *10*, 456−461.

(5) Li, C.; Hisatomi, T.; Watanabe, O.; Nakabayashi, M.; Shibata, N.; Domen, K.; Delaunay, J.-J. Positive Onset Potential and Stability of Cu_2O-Based Photocathodes in Water Splitting by Atomic Layer Deposition of a Ga_2O_3 Buffer Layer. *Energy Environ. Sci.* **2015**, *8*, 1493−1500.

(6) Niu, W.; Moehl, T.; Cui, W.; Wick-Joliat, R.; Zhu, L.; Tilley, S. D. Extended Light Harvesting with Dual Cu_2O-Based Photocathodes for High Efficiency Water Splitting. *Adv. Energy Mater.* **2018**, *8*, 1702323.

(7) Chen, S.; Wang, L.-W. Thermodynamic Oxidation and Reduction Potentials of Photocatalytic Semiconductors in Aqueous Solution. *Chem. Mater.* **2012**, *24*, 3659−3666.

(8) Morales-Guio, C. G.; Tilley, S. D.; Vrubel, H.; Grätzel, M.; Hu, X. Hydrogen Evolution from a Copper(I) Oxide Photocathode Coated with an Amorphous Molybdenum Sulphide Catalyst. *Nat. Commun.* **2014**, *5*, 3059.

DOI: 10.1021/acs.chemmater.9b00009
Chem. Mater. 2019, 31, 2524−2534

(9) Díaz-García, A. K.; Lana-Villarreal, T.; Gómez, R. Sol-gel copper chromium delafossite thin films as stable oxide photocathodes for water splitting. *J. Mater. Chem. A* **2015**, *3*, 19683−19687.
(10) Choi, S. Y.; Kim, C.-D.; Han, D. S.; Park, H. Facilitating Hole Transfer on Electrochemically Synthesized p-Type $CuAlO_2$ Films for Efficient Solar Hydrogen Production from Water. *J. Mater. Chem. A* **2017**, *5*, 10165−10172.
(11) Tablero Crespo, C. Potentiality of $CuFeO_2$-Delafossite as a Solar Energy Converter. *Sol. Energy* **2018**, *163*, 162−166.
(12) Gu, J.; Wuttig, A.; Krizan, J. W.; Hu, Y.; Detweiler, Z. M.; Cava, R. J.; Bocarsly, A. B. Mg-Doped $CuFeO_2$ Photocathodes for Photoelectrochemical Reduction of Carbon Dioxide. *J. Phys. Chem. C* **2013**, *117*, 12415−12422.
(13) Read, C. G.; Park, Y.; Choi, K.-S. Electrochemical Synthesis of p-Type $CuFeO_2$ Electrodes for Use in a Photoelectrochemical Cell. *J. Phys. Chem. Lett.* **2012**, *3*, 1872−1876.
(14) Kang, U.; Choi, S. K.; Ham, D. J.; Ji, S. M.; Choi, W.; Han, D. S.; Abdel-Wahab, A.; Park, H. Photosynthesis of Formate from CO_2 and Water at 1% Energy Efficiency via Copper Iron Oxide Catalysis. *Energy Environ. Sci.* **2015**, *8*, 2638−2643.
(15) Yang, X.; Fugate, E. A.; Mueanngern, Y.; Baker, L. R. Photoelectrochemical CO_2 Reduction to Acetate on Iron−Copper Oxide Catalysts. *ACS Catal.* **2017**, *7*, 177−180.
(16) Prévot, M. S.; Guijarro, N.; Sivula, K. Enhancing the Performance of a Robust Sol-Gel-Processed p-Type Delafossite $CuFeO_2$ Photocathode for Solar Water Reduction. *ChemSusChem* **2015**, *8*, 1359−1367.
(17) Prévot, M. S.; Li, Y.; Guijarro, N.; Sivula, K. Improving Charge Collection with Delafossite Photocathodes: A Host−Guest $CuAlO_2$/$CuFeO_2$ Approach. *J. Mater. Chem. A* **2016**, *4*, 3018−3026.
(18) Oh, Y.; Yang, W.; Kim, J.; Jeong, S.; Moon, J. Enhanced Photocurrent of Transparent $CuFeO_2$ Photocathodes by Self-Light-Harvesting Architecture. *ACS Appl. Mater. Interfaces* **2017**, *9*, 14078−14087.
(19) Jang, Y. J.; Park, Y. B.; Kim, H. E.; Choi, Y. H.; Choi, S. H.; Lee, J. S. Oxygen-Intercalated $CuFeO_2$ Photocathode Fabricated by Hybrid Microwave Annealing for Efficient Solar Hydrogen Production. *Chem. Mater.* **2016**, *28*, 6054−6061.
(20) Jin, Y.; Chumanov, G. Solution Synthesis of Pure 2H $CuFeO_2$ at Low Temperatures. *RSC Adv.* **2016**, *6*, 26392−26397.
(21) Jiang, T.; Zhao, Y.; Liu, M.; Chen, Y.; Xia, Z.; Xue, H. Enhancing the Lifetime of Photoinduced Charge Carriers in $CuFeO_2$ Nanoplates by Hydrothermal Doping of Mg for Photoelectrochemical Water Reduction. *Phys. Status Solidi* **2018**, *215*, 1800056.
(22) Galakhov, V. R.; Poteryaev, A. I.; Kurmaev, E. Z.; Anisimov, V. I.; Bartkowski, S.; Neumann, M.; Lu, Z. W.; Klein, B. M.; Zhao, T.-R. Valence-Band Spectra and Electronic Structure of $CuFeO_2$. *Phys. Rev. B: Condens. Matter Mater. Phys.* **1997**, *56*, 4584−4591.
(23) Hiraga, H.; Makino, T.; Fukumura, T.; Weng, H.; Kawasaki, M. Electronic Structure of the Delafossite-Type $CuMO_2$ (M=Sc, Cr, Mn, Fe, and Co): Optical Absorption Measurements and First-Principles Calculations. *Phys. Rev. B: Condens. Matter Mater. Phys.* **2011**, *84*, 041411.
(24) Husek, J.; Cirri, A.; Biswas, S.; Asthagiri, A.; Baker, L. R. Hole Thermalization Dynamics Facilitate Ultrafast Spatial Charge Separation in $CuFeO_2$ Solar Photocathodes. *J. Phys. Chem. C* **2018**, *122*, 11300−11304.
(25) Benko, F. A.; Koffyberg, F. P. Opto-Electronic Properties of p- and n-Type Delafossite, CuFeO2. *J. Phys. Chem. Solids* **1987**, *48*, 431−434.
(26) Prévot, M. S.; Jeanbourquin, X. A.; Bourée, W. S.; Abdi, F.; Friedrich, D.; van de Krol, R.; Guijarro, N.; Le Formal, F.; Sivula, K. Evaluating Charge Carrier Transport and Surface States in $CuFeO_2$ Photocathodes. *Chem. Mater.* **2017**, *29*, 4952−4962.
(27) Kotani, A.; Shin, S. Resonant Inelastic X-Ray Scattering Spectra for Electrons in Solids. *Rev. Mod. Phys.* **2001**, *73*, 203−246.
(28) Ament, L. J. P.; van Veenendaal, M.; Devereaux, T. P.; Hill, J. P.; van den Brink, J. Resonant Inelastic X-Ray Scattering Studies of Elementary Excitations. *Rev. Mod. Phys.* **2011**, *83*, 705−767.
(29) Cooper, J. K.; Gul, S.; Toma, F. M.; Chen, L.; Glans, P.-A.; Guo, J.; Ager, J. W.; Yano, J.; Sharp, I. D. Electronic Structure of Monoclinic $BiVO_4$. *Chem. Mater.* **2014**, *26*, 5365−5373.
(30) Jiang, C.-M.; Farmand, M.; Wu, C. H.; Liu, Y.-S.; Guo, J.; Drisdell, W. S.; Cooper, J. K.; Sharp, I. D. Electronic Structure, Optoelectronic Properties, and Photoelectrochemical Characteristics of γ-$Cu_3V_2O_8$ Thin Films. *Chem. Mater.* **2017**, *29*, 3334−3345.
(31) Guo, J.-H.; Butorin, S. M.; Wassdahl, N.; Nordgren, J.; Berastegut, P.; Johansson, L.-G. Electronic Structure of $YBa_2Cu_3O_x$ and $YBa_2Cu_4O_8$ Studied by Soft-X-ray Absorption and Emission Spectroscopies. *Phys. Rev. B: Condens. Matter Mater. Phys.* **2000**, *61*, 9140−9144.
(32) Lu, L.; Hancock, J. N.; Chabot-Couture, G.; Ishii, K.; Vajk, O. P.; Yu, G.; Mizuki, J.; Casa, D.; Gog, T.; Greven, M. Incident Energy and Polarization-Dependent Resonant Inelastic X-ray Scattering Study of La_2CuO_4. *Phys. Rev. B: Condens. Matter Mater. Phys.* **2006**, *74*, 224509.
(33) Cooper, J. K.; Reyes-Lillo, S. E.; Hess, L. H.; Jiang, C.-M.; Neaton, J. B.; Sharp, I. D. Physical Origins of the Transient Absorption Spectra and Dynamics in Thin-Film Semiconductors: The Case of $BiVO_4$. *J. Phys. Chem. C* **2018**, *122*, 20642−20652.
(34) Qiao, R.; Li, Q.; Zhuo, Z.; Sallis, S.; Fuchs, O.; Blum, M.; Weinhardt, L.; Heske, C.; Pepper, J.; Jones, M.; et al. High-Efficiency in Situ Resonant Inelastic x-Ray Scattering (iRIXS) Endstation at the Advanced Light Source. *Rev. Sci. Instrum.* **2017**, *88*, 033106.
(35) Giannozzi, P.; Baroni, S.; Bonini, N.; Calandra, M.; Car, R.; Cavazzoni, C.; Ceresoli, D.; Chiarotti, G. L.; Cococcioni, M.; Dabo, I.; et al. QUANTUM ESPRESSO: A Modular and Open-Source Software Project for Quantum Simulations of Materials. *J. Phys.: Condens. Matter* **2009**, *21*, 395502.
(36) Giannozzi, P.; Andreussi, O.; Brumme, T.; Bunau, O.; Buongiorno Nardelli, M.; Calandra, M.; Car, R.; Cavazzoni, C.; Ceresoli, D.; Cococcioni, M.; et al. Advanced Capabilities for Materials Modelling with Quantum ESPRESSO. *J. Phys.: Condens. Matter* **2017**, *29*, 465901.
(37) Perdew, J. P.; Burke, K.; Ernzerhof, M. Generalized Gradient Approximation Made Simple. *Phys. Rev. Lett.* **1996**, *77*, 3865−3868.
(38) Liechtenstein, A. I.; Anisimov, V. I.; Zaanen, J. Density-Functional Theory and Strong Interactions: Orbital Ordering in Mott-Hubbard Insulators. *Phys. Rev. B: Condens. Matter Mater. Phys.* **1995**, *52*, R5467−R5470.
(39) Cococcioni, M.; de Gironcoli, S. Linear Response Approach to the Calculation of the Effective Interaction Parameters in the LDA+U Method. *Phys. Rev. B: Condens. Matter Mater. Phys.* **2005**, *71*, 035105.
(40) Kimura, T.; Lashley, J. C.; Ramirez, A. P. Inversion-Symmetry Breaking in the Noncollinear Magnetic Phase of the Triangular-Lattice Antiferromagnet $CuFeO_2$. *Phys. Rev. B: Condens. Matter Mater. Phys.* **2006**, *73*, 220401.
(41) Vanderbilt, D. Soft Self-Consistent Pseudopotentials in a Generalized Eigenvalue Formalism. *Phys. Rev. B: Condens. Matter Mater. Phys.* **1990**, *41*, 7892−7895.
(42) Hinuma, Y.; Pizzi, G.; Kumagai, Y.; Oba, F.; Tanaka, I. Band Structure Diagram Paths Based on Crystallography. *Comput. Mater. Sci.* **2017**, *128*, 140−184.
(43) Liang, Y.; Vinson, J.; Pemmaraju, S.; Drisdell, W. S.; Shirley, E. L.; Prendergast, D. Accurate X-ray Spectral Predictions: An Advanced Self-Consistent-Field Approach Inspired by Many-Body Perturbation Theory. *Phys. Rev. Lett.* **2017**, *118*, 096402.
(44) Liang, Y.; Prendergast, D. Quantum Many-Body Effects in X-ray Spectra Efficiently Computed Using a Basic Graph Algorithm. *Phys. Rev. B* **2018**, *97*, 205127.
(45) Pavunny, S. P.; Kumar, A.; Katiyar, R. S. Raman Spectroscopy and Field Emission Characterization of Delafossite $CuFeO_2$. *J. Appl. Phys.* **2010**, *107*, 013522.
(46) Bourée, W. S.; Prévot, M. S.; Jeanbourquin, X. A.; Guijarro, N.; Johnson, M.; Formal, F. L.; Sivula, K. Robust Hierarchically Structured Biphasic Ambipolar Oxide Photoelectrodes for Light-Driven Chemical Regulation and Switchable Logic Applications. *Adv. Mater.* **2016**, *28*, 9308−9312.

DOI: 10.1021/acs.chemmater.9b00009
Chem. Mater. 2019, 31, 2524−2534

(47) Hiraga, H.; Makino, T.; Fukumura, T.; Ohtomo, A.; Kawasaki, M. Excitonic Characteristics in Direct Wide-Band-Gap $CuScO_2$ Epitaxial Thin Films. *Appl. Phys. Lett.* **2009**, *95*, 211908.
(48) Ambacher, O.; Rieger, W.; Ansmann, P.; Angerer, H.; Moustakas, T. D.; Stutzmann, M. Sub-Bandgap Absorption of Gallium Nitride Determined by Photothermal Deflection Spectroscopy. *Solid State Commun.* **1996**, *97*, 365−370.
(49) Lany, S. Semiconducting Transition Metal Oxides. *J. Phys.: Condens. Matter* **2015**, *27*, 283203.
(50) Rettie, A. J. E.; Chemelewski, W. D.; Emin, D.; Mullins, C. B. Unravelling Small-Polaron Transport in Metal Oxide Photoelectrodes. *J. Phys. Chem. Lett.* **2016**, *7*, 471−479.
(51) Ziwritsch, M.; Müller, S.; Hempel, H.; Unold, T.; Abdi, F. F.; van de Krol, R.; Friedrich, D.; Eichberger, R. Direct Time-Resolved Observation of Carrier Trapping and Polaron Conductivity in $BiVO_4$. *ACS Energy Lett.* **2016**, *1*, 888−894.
(52) Carneiro, L. M.; Cushing, S. K.; Liu, C.; Su, Y.; Yang, P.; Alivisatos, A. P.; Leone, S. R. Excitation-Wavelength-Dependent Small Polaron Trapping of Photoexcited Carriers in α-Fe_2O_3. *Nat. Mater.* **2017**, *16*, 819−825.
(53) Ong, K. P.; Bai, K.; Blaha, P.; Wu, P. Electronic Structure and Optical Properties of $AFeO_2$ (A = Ag, Cu) within GGA Calculations. *Chem. Mater.* **2007**, *19*, 634−640.
(54) Eyert, V.; Frésard, R.; Maignan, A. Long-Range Magnetic Order and Spin-Lattice Coupling in Delafossite $CuFeO_2$. *Phys. Rev. B: Condens. Matter Mater. Phys.* **2008**, *78*, 052402.
(55) Yeh, J. J.; Lindau, I. Atomic subshell photoionization cross sections and asymmetry parameters: $1 \leq Z \leq 103$. *At. Data Nucl. Data Tables* **1985**, *32*, 1−155.
(56) Grioni, M.; van Acker, J. F.; Czyżyk, M. T.; Fuggle, J. C. Unoccupied Electronic Structure and Core-Hole Effects in the X-ray-Absorption Spectra of Cu_2O. *Phys. Rev. B: Condens. Matter Mater. Phys.* **1992**, *45*, 3309−3318.
(57) Jiang, P.; Prendergast, D.; Borondics, F.; Porsgaard, S.; Giovanetti, L.; Pach, E.; Newberg, J.; Bluhm, H.; Besenbacher, F.; Salmeron, M. Experimental and Theoretical Investigation of the Electronic Structure of Cu_2O and CuO Thin Films on Cu(110) Using X-ray Photoelectron and Absorption Spectroscopy. *J. Chem. Phys.* **2013**, *138*, 024704.
(58) Miedema, P. S.; de Groot, F. M. F. The Iron L Edges: Fe 2p X-ray Absorption and Electron Energy Loss Spectroscopy. *J. Electron Spectrosc. Relat. Phenom.* **2013**, *187*, 32−48.
(59) Gilbert, B.; Frandsen, C.; Maxey, E. R.; Sherman, D. M. Band-Gap Measurements of Bulk and Nanoscale Hematite by Soft X-ray Spectroscopy. *Phys. Rev. B: Condens. Matter Mater. Phys.* **2009**, *79*, 035108.
(60) Cooper, J. K.; Gul, S.; Toma, F. M.; Chen, L.; Liu, Y.-S.; Guo, J.; Ager, J. W.; Yano, J.; Sharp, I. D. Indirect Bandgap and Optical Properties of Monoclinic Bismuth Vanadate. *J. Phys. Chem. C* **2015**, *119*, 2969−2974.
(61) Miyawaki, J.; Suga, S.; Fujiwara, H.; Urasaki, M.; Ikeno, H.; Niwa, H.; Kiuchi, H.; Harada, Y. Dzyaloshinskii-Moriya Interaction in α-Fe_2O_3 Measured by Magnetic Circular Dichroism in Resonant Inelastic Soft X-ray Scattering. *Phys. Rev. B* **2017**, *96*, 214420.
(62) Vayssieres, L.; Sathe, C.; Butorin, S. M.; Shuh, D. K.; Nordgren, J.; Guo, J. One-Dimensional Quantum-Confinement Effect in α-Fe_2O_3 Ultrafine Nanorod Arrays. *Adv. Mater.* **2005**, *17*, 2320−2323.

DOI: 10.1021/acs.chemmater.9b00009
Chem. Mater. 2019, 31, 2524−2534